

Bubble-Pair Propelled Colloidal Kayaker

Yingjie Wu,[†] Tiejian Si,^{*,†} Changyong Gao,[†] Mingcheng Yang,^{‡,§} and Qiang He^{*,†}

[†]Key Laboratory of Microsystems and Microstructures Manufacturing, Ministry of Education, Harbin Institute of Technology, Yi Kuang Jie 2, Harbin 150080, China

[‡]Institute of Physics, Chinese Academy of Sciences, Beijing 100190, China

[§]University of Chinese Academy of Sciences, Beijing 100049, China

Supporting Information

ABSTRACT: We report a hollow dumbbell-shaped manganese dioxide (MnO₂) colloidal kayaker capable of converting a pair of breathing oxygen bubbles into self-propelled movement. The bubble pair generated by catalytic decomposition of hydrogen peroxide fuel grew either synchronously or asynchronously, driving the colloidal kayaker to move along a fluctuating circle. The synchronous or asynchronous breathing mode of bubble pair is governed by the asymmetric catalytic sites of the colloidal kayakers. This imbalanced distribution of bubble propulsion force generates the driving force and the centripetal force on the colloidal kayaker. The dynamics of colloidal kayakers is well-described by the overdamped Langevin equation and fluid field simulation. Such bubble-pair propelled colloidal kayakers could advance applications of catalytic nanomotors, offering effective implementation for diverse tasks for a wide range of practical applications.

Colloidal motors are micro- or nanosized machines that can perform complex tasks while being self-propelled in fluids such as cargo loading/unloading and transport,^{1–4} medical imaging,⁵ environmental remediation,⁶ sensing⁷ as well as micro/nano assembly and fabrication.^{8,9} In particular, remarkable advances have been made in the development of chemically powered colloidal motors, including Janus microparticles,^{10–15} asymmetrical tubular microengines,^{16–18} bimetallic catalytic nanorods,¹⁹ nanowires,²⁰ metal–organic frameworks^{21,22} and biomimetic microrobotics,^{23–25} which can convert locally supplied chemical fuels into movement along with precise speed regulation and spatial motion control.^{26,27} The motion of these active colloidal motors is mainly attributed to three propulsion mechanisms: self-electrophoresis,²⁸ self-diffusiophoresis,²⁹ and bubble propulsion.^{30,31} Among them, single bubble propelled Janus motors and microjets that releasing a macroscopic bubble train provides the driving force for motor movement have been widespread reported in the past decade and the detailed mechanism of motion has been reported previously.^{32–36} Single bubble propelled motors mimic the movement of some biological systems at low Reynold number condition, for instance, cyanobacteria blue-green algae swim by extruding the slime through nozzle-like organelles.³⁷ Also, two-engine mode motion in nature (e.g., penguin) exists widely, and thus two-

engine colloidal motors with two-lobed bubble erupting may mimic their motion and become a new kind of driving mode of artificial micro/nanomotors. However, to our best knowledge, bubble-pair propelled synthetic colloidal motors have been not reported yet.

In this work, we demonstrated the first example of a dumbbell-shaped hollow manganese dioxide (MnO₂) colloidal kayaker propelled by oxygen bubble pair. The hollow MnO₂ colloidal kayaker could catalytically decompose hydrogen peroxide fuel to oxygen. Because of its dumbbell-shaped geometry, two breathing oxygen bubbles generated on the waist of the particle which either grows synchronously or asynchronously to propel the motor to move in fluid. We proposed a physical model based on detailed analysis and statistics of the bubble growth and release process, which is in agreement with the experimental observation.

The dumbbell-shaped hollow MnO₂ colloidal kayakers were synthesized by hydrothermal synthesis method according to a previously report method.³⁸ Briefly, as illustrated in [Figure S1](#), the manganese carbonate dumbbell precursor was first prepared by mixing manganese chloride, sodium citrate and ammonium hydroxide and heat for 2 h at 160 °C. After the resulting precursor was preoxidized and treated by hydrochloric acid, the dumbbell-shaped hollow MnO₂ colloidal particles were obtained. The details were described in the [Supporting Information](#). The scanning electron microscopy (SEM) image in [Figure 1a](#) shows that the length of MnO₂ colloidal kayaker is about 10 μm and a cross-sectional diameter of about 2 μm. The inset image of a cracked colloidal kayaker obviously displays the hollow bells. The transmission electron microscopy (TEM) image in [Figure 1b](#) further confirms the hollow structure of as-prepared colloidal kayakers. The X-ray diffraction (XRD, [Figure S2](#)) shows that the as-prepared colloidal kayakers were composed of hexagonal MnO₂. Time-lapse optical images in [Figure 1c](#), captured from [Video S1](#), show that the colloidal kayaker could move at a speed of 22 μm/s in 10% hydrogen peroxide (H₂O₂) solution under a bubble pair propulsion. The two flapping bubbles act as paddles for swimming in fluid, which grow at the two growing points oppositely distributed above the waist of colloidal kayaker. Furthermore, the motion video of multiple motors ([Video S3](#)) and analysis ([Figure S3](#)) display that more than 70% colloidal motors propelled by a pair of breathing oxygen

Received: June 26, 2018

Published: September 4, 2018

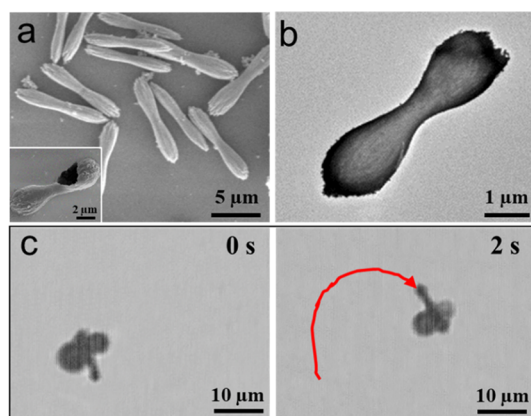


Figure 1. (a) SEM and (b) TEM images of the dumbbell-shaped manganese dioxide colloidal kayakers. The inset image displayed their hollow interior. (c) Time-lapse optical images of a dumbbell-shaped colloidal kayaker moving at 10% H_2O_2 .

bubble pairs, suggesting that bubble propelled colloidal kayaker is a common existence in our dumbbell-shaped hollow MnO_2 colloidal motors. Obviously, this movement mode is completely different from those single bubble driven motors.²¹

To better explore the propulsion dynamics of oxygen bubbles pair, we recorded the trajectory of colloidal kayakers in a relatively low concentration of H_2O_2 (5%) (Figure 2a,b and Video S2) so that the detailed evolution process of the bubble pair could be captured. For the synchronously breathing bubble pair, the average radius of the circular trajectory is about $15 \mu\text{m}$ (Figure 2a). For the asynchronously growing bubble pair, the average radius of the circular trajectory is about $12.5 \mu\text{m}$ (Figure 2b). It suggests that the asynchronous motion draws a smaller circle than that of the synchronous motion, in agreement with the statistics on circle diameter (Figure S4a,b). The measured average speed of this colloidal kayaker for the asynchronous and synchronous modes is 9.1 and $6.67 \mu\text{m/s}$, respectively, which is identical with the statistical results (Figure S4c,d). It suggests that two asynchronously growing bubbles drive the colloidal kayaker to move faster than that of two synchronously growing bubbles. In the synchronous mode, the maximum diameter for each oxygen bubble to detach from the colloidal kayaker is about $4.43 \mu\text{m}$ (Figure 2c), which is obviously smaller than that of the asynchronous mode, i.e., $5.67 \mu\text{m}$ (Figure 2d). This phenomenon can be understood by mass conservation. Because the as-generated oxygen around the colloidal kayaker is roughly constant, one bubble thus collects more oxygen molecules to reach a bigger diameter, but the other bubble would gather less. In contrast, two bubbles in the synchronous mode accumulate the equal amount of oxygen molecules instantaneously. The measured periodicity of lifetime of the big bubbles in the asynchronous mode is 2.94 fps, whereas 3.12 fps in the synchronous mode (Figure 2c,d). Obviously, the radius of two growing bubbles in both the synchronous and asynchronous modes oscillated like a sawtooth wave. Consequently, the measured instantaneous speed curve shows a sharp peak at the instance of each bubble release (Figure 2e,f).

The reaction force on the bubble passes the bubble center and points toward the bubble growing point (indicated by the red arrow in Figure 3a). The reaction force has nonzero projections both to the tangential axis (long axis) and radial

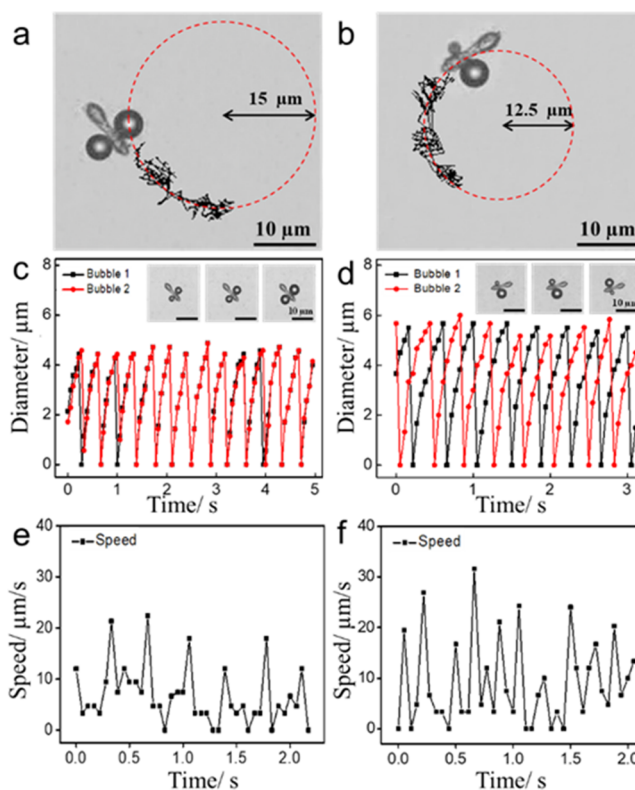


Figure 2. (a) Trajectory of a colloidal kayaker under propulsion of two synchronously growing bubbles. (b) Trajectory of the colloidal kayaker under the propulsion of two asynchronously growing bubbles. (c) Measured oscillating diameters of the two synchronously growing bubble. (d) Instantaneous bubble diameters of two asynchronously growing bubbles. Black data represents the bubble 1, red data represents bubble 2. The insets show the optical images of the two bubble growth mode. (e) Measured tangential speed of colloidal kayaker center for the synchronously growing bubble pair. (f) Measured speed of micromotor center for the asynchronous mode.

axis, which contributed the driving force and torque on the colloidal kayaker, respectively. The driving force pushes the colloidal kayaker to move forward, whereas the torque turns its direction as it moves. The tangential speeds of colloidal kayaker for the asynchronous and synchronous modes in Figure 2 are 3.42 and $2.79 \mu\text{m/s}$, respectively. The motion of the colloidal kayaker is governed by a pair of stochastic Langevin equations (more details, see Supporting Information, Equations S1, S2). The two self-propulsion force components, F_L and F_R , can be roughly quantified by Stokes' formula, $F_L = F_R = 6\pi\mu R_a V_a$, which describes the steady motion of a moving bubble in water. The measured bubble growth velocity is $V_a = 14.4 \mu\text{m/s}$ (a bubble grows to the maximum diameter of $5.75 \mu\text{m}$ in 0.4 s). The angle between the left (right) force vector and radial axis is $\theta_L = 18^\circ$ ($\theta_R = 160^\circ$). Then the tangential and radial driving forces are estimated as $F_T = 0.23 \times 10^{-12}$ N and $F_N = 0.4 \times 10^{-14}$ N. Balancing the driving force and the viscous friction, the self-propelled velocity along the long axis is determined as $V_T = 6.1 \mu\text{m/s}$, comparable to the above-mentioned experimental result. Nevertheless, in the radial direction the mean self-propelled velocity is $V_N = 0.08 \mu\text{m/s}$, which is much smaller than V_T and thus ignored. Moreover, with the position vector $r_L = 6.4 \mu\text{m}$, $r_R = 8.4 \mu\text{m}$ and the related orientation angle that are measured in experiments (Figure 3b), the driving torque is estimated as $T = F_L \times 6.4 \times$

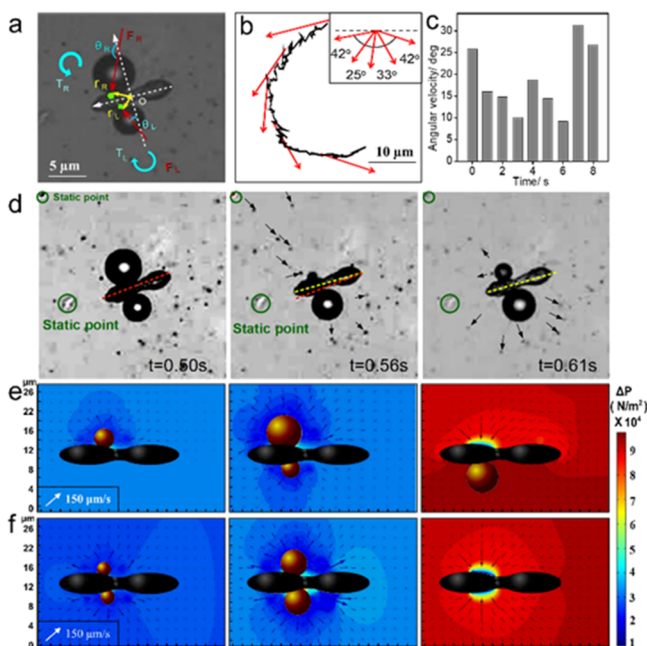


Figure 3. (a) Two sites for bubble growth and the angles for two propulsion force vectors according to the video in supplementary at 0.02 s. The yellow arrows represent the position vector from “O” (the mass center). The red vector represents the left (F_L) and right force vectors (F_R). The two angles are denoted by “ θ_L ” and “ θ_R ”. (b) Tangential vector of velocity along a recorded trajectory. (c) Measured angular velocity based on the recorded colloidal kayaker trajectory. (d) Velocity of impurities suspended in the fluid during bubble growth. Two static points attached to the substrate are chosen as reference point. The black arrow indicates the displacement vectors of these impurity particles. (e) Simulated velocity field (dark vectors) and pressure (rainbow colors) around the asynchronously growing bubble pair (the orange ball) for three different stages: the generation of small bubble (the left), the growing bubble (the middle), and the explosion of bubble (the right). The length of the black arrow is proportional to the magnitude of velocity of liquid flow. (f) Flow field and pressure distribution around the synchronously growing bubble pair for the three different stages.

$\sin(112^\circ) - F_R \times 8.4 \times \sin(93^\circ) = -0.85 \times 10^{-18}$ N·m. Here, the clockwise is defined as positive direction. As a consequence, the computed angular speed is about $\omega = 34^\circ/\text{s}$. This theoretical angular velocity is slightly higher than the fluctuating experiment value of angular velocity, $\omega = 10\text{--}31^\circ/\text{s}$ (Figure 3b,c). This small mismatch is most likely due to the bubble size fluctuations caused by oxygen molecules. The orbital radius in a circular motion is $V_T/\omega = 9.1 \mu\text{m}$, which is consistent with the above experimental measurement. Note that the fluctuating bubble growth speed results in a constantly fluctuating velocity of the colloidal kayaker and also a time-varying angular velocity.

Time-lapsed images in Figure 3d clearly reveal that at the instantaneous detachment of the right bubble, $t = 0.56$ s, the impurities were attracted to the bubble growing position by the fluid flow, and the colloidal kayaker suddenly jumped over a short distance to the right side of tangential vector. When the right bubble began to grow bigger from a baby bubble, at $t = 0.61$ s, the impurity particles were pushed away from the colloidal kayaker, and the colloidal kayaker was pushed to the left side of tangential vector.

The flow field was simulated by using the fluid dynamics to quantify the distribution of pressure (Figure 3e,f). For the

asynchronous case, the right big bubble was surrounded by a bigger area with strong flow than that around the small left bubble (Figure 3e). So, the fluid around the right bubble applies a bigger pressure on the colloidal kayaker than the left one. Once the right bubble detaches at its critical radius, the pressure of the right bubble suddenly drops to zero, the surrounding fluid were pushed to the center of released bubble by hydraulic pressure (Figure 3e, the right box). Then the left small bubble induces a stronger reaction force of surroundings. For the synchronous case, the flow field for growing bubble and released bubble were similar to that of asynchronous case. Most of the reaction force vectors canceled each other in the direction perpendicularly to the long axis of the colloidal kayaker (Figure 3f). Hence, the colloidal kayaker was pushed forward in the direction along the long axis. Note that the fast flow near the surface of the colloidal kayaker is induced by the narrow space between the contacting surface of bubbles and the colloidal kayaker.

In conclusion, we have demonstrated a dumbbell-shaped manganese dioxide colloidal kayaker propelled by a pair of oxygen bubbles generated by catalytic decomposition of hydrogen peroxide fuel. We analyzed the bubble pair growth mode and movement behaviors of the colloidal kayaker, and developed a physical model based on bubble growth dynamic and equation of motion for microparticles. Synchronous or asynchronous bubble pair growing mode leads to apparent different behaviors. The two-growing sites of the bubble pair behaves like a seesaw, as they are located at the two ending point of the diameter in the radial cross section. Such bubble-pair propelled colloidal kayakers offer a new mechanism to control the motion of colloidal particles, and thus, are promising for far-reaching implications in nanomachinery, biomedicine, cargo targeted transport, and chemical sensing.

■ ASSOCIATED CONTENT

📄 Supporting Information

The Supporting Information is available free of charge on the ACS Publications website at DOI: 10.1021/jacs.8b06646.

Experimental details, theoretical section (PDF)

Motion of a micro-dumbbell manganese dioxide colloidal kayaker at 10% H_2O_2 (AVI)

Circular motion of a micro-dumbbell colloidal kayaker with synchronously or asynchronously growing bubble pair at 5% H_2O_2 (AVI)

Self-propelled motion of colloidal kayakers at 10% H_2O_2 (AVI)

■ AUTHOR INFORMATION

Corresponding Authors

*tieyansi@hit.edu.cn

*qianghe@hit.edu.cn

ORCID

Qiang He: 0000-0002-3557-6865

Notes

The authors declare no competing financial interest.

■ ACKNOWLEDGMENTS

This work was financially supported by the National Nature Science Foundation of China (21573053, 11404379, 11674365).

■ REFERENCES

- (1) Wang, J. *Nanomachines: Fundamentals and Applications*; Wiley-VCH: Weinheim, Germany, 2013.
- (2) Wang, H.; Pumera, M. *Chem. Rev.* **2015**, *115*, 8704–8735.
- (3) Manjare, M.; Yang, B.; Zhao, Y. P. *Phys. Rev. Lett.* **2012**, *109*, 128305.
- (4) Mei, Y. F.; Solovev, A. A.; Sanchez, S.; Schmidt, O. G. *Chem. Soc. Rev.* **2011**, *40*, 2109–2119.
- (5) Vilela, D.; Cossio, U.; Parmar, J.; Martínez-Villacorta, A. M.; Gomez-Vallejo, V.; Llop, J.; Sánchez, S. *ACS Nano* **2018**, *12*, 1220–1227.
- (6) Gao, W.; Wang, J. *ACS Nano* **2014**, *8*, 3170–3180.
- (7) Jurado-Sánchez, B.; Escarpa, A. *Electroanalysis* **2017**, *29*, 14–23.
- (8) Li, T.; Chang, X.; Wu, Z.; Li, J.; Shao, G.; Deng, X.; Qiu, J.; Guo, B.; Zhang, G.; He, Q.; Li, L.; Wang, J. *ACS Nano* **2017**, *11*, 9268–9275.
- (9) Wang, W.; Castro, L. A.; Hoyos, M.; Mallouk, T. E. *ACS Nano* **2012**, *6*, 6122–6132.
- (10) Gibbs, J. G.; Zhao, Y. P. *Appl. Phys. Lett.* **2009**, *94*, 163104.
- (11) Wilson, D. A.; Nolte, R. J.; van Hest, J. C. *Nat. Chem.* **2012**, *4*, 268–274.
- (12) Ma, X.; Hahn, K.; Sanchez, S. *J. Am. Chem. Soc.* **2015**, *137*, 4976–4979.
- (13) Mou, F. Z.; Chen, C. R.; Ma, H. R.; Yin, Y. X.; Wu, Q. Z.; Guan, J. G. *Angew. Chem., Int. Ed.* **2013**, *52*, 7208–7212.
- (14) Wu, Y. J.; Wu, Z. G.; Lin, X. K.; He, Q.; Li, J. B. *ACS Nano* **2012**, *6*, 10910–10916.
- (15) Gao, W.; Pei, A.; Dong, R. F.; Wang, J. *J. Am. Chem. Soc.* **2014**, *136*, 2276–2279.
- (16) Xu, T. L.; Soto, F.; Gao, W.; Garcia-Gradilla, V.; Li, J. X.; Zhang, X. J.; Wang, J. *J. Am. Chem. Soc.* **2014**, *136*, 8552–8555.
- (17) Li, J.; Liu, W.; Wang, J.; Rozen, I.; He, S.; Chen, C.; Kim, H. G.; Lee, H.-J.; Lee, H.-B.-R.; Kwon, S.-H.; Li, T.; Li, L.; Wang, J.; Mei, Y. *Adv. Funct. Mater.* **2017**, *27*, 1700598.
- (18) Mou, F.; Li, Y.; Chen, C.; Li, W.; Yin, Y.; Ma, H.; Guan, J. *Small* **2015**, *11*, 2564–2570.
- (19) Gao, W.; Dong, R. F.; Thamphiwatana, S.; Li, J. X.; Gao, W. W.; Zhang, L. F.; Wang, J. *ACS Nano* **2015**, *9*, 117–123.
- (20) Gao, W.; Manesh, K. M.; Hua, J.; Sattayasamitsathit, S.; Wang, J. *Small* **2011**, *7*, 2047–2051.
- (21) Li, J. X.; Yu, X.; Xu, M. L.; Liu, W. J.; Sandraz, E.; Lan, H.; Wang, J.; Cohen, S. M. *J. Am. Chem. Soc.* **2017**, *139*, 611–614.
- (22) Ikezoe, Y.; Washino, G.; Uemura, T.; Kitagawa, S.; Matsui, H. *Nat. Mater.* **2012**, *11*, 1081–1085.
- (23) Zhu, W.; Li, J. X.; Leong, Y. J.; Rozen, I.; Qu, X.; Dong, R. F.; Wu, Z. G.; Gao, W.; Chung, P. H.; Wang, J.; Chen, S. C. *Adv. Mater.* **2015**, *27*, 4411–4417.
- (24) Qiu, T.; Lee, T. C.; Mark, A. G.; Morozov, K. I.; Munster, R.; Mierka, O.; Turek, S.; Leshansky, A. M.; Fischer, P. *Nat. Commun.* **2014**, *5*, 5119.
- (25) Servant, A.; Qiu, F.; Mazza, M.; Kostarelos, K.; Nelson, B. *Adv. Mater.* **2015**, *27*, 2981–2988.
- (26) Medina-Sánchez, M.; Schwarz, L.; Meyer, A. K.; Hebenstreit, F.; Schmidt, O. G. *Nano Lett.* **2016**, *16*, 555–561.
- (27) Sánchez, S.; Soler, L.; Katuri, J. *Angew. Chem., Int. Ed.* **2015**, *54*, 1414–1444.
- (28) Lee, T.-C.; Alarcón-Correa, M.; Miksch, C.; Hahn, K.; Gibbs, J. G.; Fischer, P. *Nano Lett.* **2014**, *14*, 2407–2412.
- (29) Golestanian, R. *Phys. Rev. Lett.* **2009**, *102*, 188305.
- (30) Wang, H.; Zhao, G. J.; Pumera, M. *J. Am. Chem. Soc.* **2014**, *136*, 2719–2722.
- (31) Wang, H.; Moo, J. G. S.; Pumera, M. *ACS Nano* **2016**, *10*, 5041–5050.
- (32) Ismagilov, R. F.; Schwartz, A.; Bowden, N.; Whitesides, G. M. *Angew. Chem., Int. Ed.* **2002**, *41*, 652–654.
- (33) Wu, Y. J.; Wu, Z. G.; Lin, X. L.; He, Q.; Li, J. B. *ACS Nano* **2012**, *6*, 10910–10916.
- (34) Nakata, S.; Nomura, M.; Yamamoto, H.; Izumi, S.; Suematsu, N. J.; Ikura, Y.; Amemiya, T. *Angew. Chem., Int. Ed.* **2017**, *56*, 861–864.
- (35) Mei, Y.; Huang, G.; Solovev, A. A.; Ureña, E. B.; Mönch, I.; Ding, F.; Reindl, T.; Fu, R. K. Y.; Chu, P. K.; Schmidt, O. G. *Adv. Mater.* **2008**, *20*, 4085–4090.
- (36) Solovev, A. A.; Mei, Y.; Bermúdez Ureña, E.; Huang, G.; Schmidt, O. G. *Small* **2009**, *5*, 1688–1692.
- (37) Lauga, E.; Powers, T. R. *Rep. Prog. Phys.* **2009**, *72*, 096601.
- (38) Fei, J. B.; Cui, Y.; Yan, X. H.; Qi, W.; Yang, Y.; Wang, K. W.; He, Q.; Li, J. B. *Adv. Mater.* **2008**, *20*, 452–456.